Numerical Study of Iced Airfoils with Horn Features Using Large-Eddy Simulation

Maochao Xiao* and Yufei Zhang[†]

Tsinghua University, 100084 Beijing, People's Republic of China

and

Feng Zhou[‡]

Shanghai Aircraft Design and Research Institute, 201210 Shanghai, People's Republic of China

Separated flowfields around two iced airfoils with horn features near stall are numerically studied using wall-modeled large-eddy simulation. The iced airfoils are the GLC305 airfoil with rime ice 212 and the NLF0414 airfoil with glaze ice 623. A grid-quality-based hybrid central/upwind scheme is applied for numerical flux computation. The close agreement between the computed lift, drag, and surface pressure distribution and the experimental results illustrates the capability of the present method. In particular, the current method can accurately predict the Kelvin–Helmholtz instability of a free shear layer. The statistical results, instantaneous flowfields, pressure fluctuations, and characteristic frequencies are investigated. Both flowfields are dominated by separation bubbles. The bubble length increases with the angle of attack according to a quadratic relation. A strong-fluctuation region in the flowfield grows rapidly at high angles of attack, especially near stall. High- and low-frequency peaks are found in the initial and further downstream regions of the free shear layer, respectively. The high frequency is caused by the Kelvin–Helmholtz instability and vortex shedding. The low frequency might be caused by the vortex merging in the further downstream region of the free shear layer.

Nomenclature

C_D	=	drag coefficient
C_L	=	lift coefficient
$C_{L,\mathrm{rms}}$	=	rms of lift coefficient
C_p	=	pressure coefficient
$C_{p,\mathrm{rms}}$	=	rms of pressure coefficient
c	=	airfoil chord length
f	=	frequency
Ma	=	Mach number
P_∞	=	freestream pressure
Q	=	second invariant of the velocity gradient tensor
R	=	spanwise correlation
Re	=	Reynolds number
U	=	time-averaged velocity
U_∞	=	freestream velocity
u	=	instantaneous x velocity
y_{surf}	=	y coordinate of airfoil surface
Φ_{pp}	=	power spectral density of pressure
Ω_z	=	spanwise vorticity

I. Introduction

NUMEROUS flight accidents have shown that ice accretions during critical weather conditions can result in severe reductions in maximum lift coefficient and control surface effectiveness and a substantial increase in drag coefficient for an aircraft [1]. Even an inconspicuous ice accretion on the leading edge of an airfoil can reduce the lift by 40% and increase the drag by 50% [2].

Several researchers [2–4] conducted systematic icing tests and documented the ice shapes formed on three modern airfoils: those used on a civilian aircraft, a business jet aircraft, and a general aviation aircraft. Addy and Chung [2] also studied the influence of ice accretions on the aerodynamic performance, and found that the presence of ice overrides the viscous forces acting on the normal boundary layer of an airfoil. The effects of Reynolds number and Mach number on the maximum lift coefficient, stall angle of attack (AOA), and pressure distribution are small for an iced airfoil [2,3]. Particle-image-velocimetry measurement and oil-flow visualization results [5,6] also showed that three-dimensional (3-D) ice accretions with spanwise variation and jaggedness cause reattachment to occur earlier than two-dimensional (2-D) ice accretion. The separation bubble behind the ice horn is the dominant mechanism for both the mean flow and fluctuations. Ansell and Bragg [7] identified three fluctuation modes for a NACA 0012 airfoil with a 3.5 min ice accretion. Two of these modes are associated with the separation bubble: a vortex motion mode and a shear-layer flapping mode. The third mode is a low-frequency mode caused by the thin-airfoil stall behavior. Bragg et al. [8] and Lynch and Khodadoust [1] systematically reviewed the aerodynamic performance, and reported the degradation caused by various types of ice accretions on the lifting surfaces of fixed-wing aircraft.

Numerical simulation is an effective method for investigating the flow details of the stall behavior of an iced airfoil. The Reynolds-averaged Navier–Stokes (RANS) method has been widely employed for aerodynamic-performance evaluation. However, this method tends to overpredict the upper surface pressure and underpredict the lift coefficient and the stall angle [9–11], because RANS cannot correctly predict the separation-bubble length aft of the ice horn, especially in the cases, in which the bubble dominates the upper surface flow at a large AOA. Many researchers adopted advanced turbulence-simulation techniques to compute the performance of iced airfoils. Brown et al. [12] used an implicit-large-eddy-simulation (ILES) method, and showed that both the small-scale and large-scale geometric features of the ice shape motivate rich, unsteady turbulent flow structures. Because the grid requirement of the ILES in the boundary layer is comparable to direct numerical simulation, hybrid RANS/large-eddy simulation (LES) methods, such as detached-eddy simulation (DES), zonal DES (ZDES), dynamic hybrid RANS/LES

*Graduate Student, School of Aerospace Engineering. Student Member AIAA.

[†]Associate Professor; zhangyufei@tsinghua.edu.cn. Senior Member AIAA (Corresponding Author).

[‡]Senior Engineer.

method (DHRL), etc., are employed by researchers to study iced airfoils. Pan and Loth [13] reported that the DES method predicts more consistent maximum lift coefficient and stall angle with experimental data than RANS if the grid resolution is sufficient. Other studies also demonstrated the improvement of lift and drag coefficients predicted using DES-type methods [14–16]. However, Alam et al. [17] and Xiao et al. [18] reported that DES-type methods cannot effectively predict the Kelvin–Helmholtz (K–H) instability of a free mixing shear layer, which delays the reattachment point behind the ice horn and leads to a longer separation bubble and lower-pressure plateau if the grid resolution is insufficient. Alam et al. [17] used the DHRL method to accelerate the K–H instability, and Xiao et al. [18] applied a new numerical scheme with controllable dissipation to promote the K–H instability. Both methods provided more consistent agreements with experimental data than the baseline DES-type methods, revealing that resolving the K–H instability is a key issue for accurately predicting the separation bubble of an iced airfoil. Duclercq et al. [19] and Zhang et al. [20] adopted the ZDES method to study iced airfoils, and found a characteristic frequency in the free mixing shear layer. In addition, they showed that the power-spectral-density (PSD) magnitude of streamwise velocity gradually decreases as the turbulent flow develops downward due to the transition of resolved kinetic energy into internal energy.

In an unsteady turbulence simulation, reducing the numerical dissipation is helpful for resolving more turbulent structures [21]. A weighted blending of a dissipative upwind flux and a nondissipative central flux is often applied for turbulence simulation. Previously, the blending parameter was a small constant [22] or a variable based on experience [23] or a selected flowfield feature [24]. However, the parameter used depends on the solver characteristics and the user's experience, and the process is usually time consuming.

In this paper, a wall-modeled LES (WMLES) method is adopted to study the flow near stall conditions around two iced airfoils, which are the GLC305 airfoil with 212 rime ice (GLC305/212) [3] and the NLF0414 airfoil with 623 glaze ice (NLF0414/623) [2]. Both iced airfoils feature horns at the leading edges. A low-dissipation blending central/upwind scheme is employed to simulate the turbulent flowfields. The blending parameter is precomputed based on the local grid quality or the reconstruction error [25,26]. Numerical results are compared with the experimental data provided by several researchers [2–4,27]. The turbulent flowfields are studied in terms of mean flow and fluctuations. In particular, the influence of the incidence angle on the statistical and instantaneous flowfields is investigated. Characteristic frequencies in the free shear layer of the ice horn and near the reattachment behind the separation bubble are analyzed in detail.

II. Computational Method and Problem Description

A. Computational Method

In the present study, the Navier–Stokes equations are solved using an in-house structured code [28–30]. The solver is fully parallelized using the message-passing-interface technique. The third-order Runge–Kutta method is used for temporal integration. The viscous term is discretized via a second-order central scheme. In the following, the grid-quality-based hybrid central/upwind scheme, the subgrid-scale model, and the wall model used in this paper are briefly introduced [25,26,31,32].

In an unsteady turbulence simulation, the numerical dissipation is a significant factor affecting the resolution of turbulent structures. In this paper, the inviscid flux is computed by applying a blend of a nondissipative central scheme and a dissipative upwind scheme. The blending flux is expressed as

$$F_{\text{inviscid}} = (1 - \sigma)F_{\text{central}} + \sigma F_{\text{upwind}} \qquad (1)$$

in which the blending parameter $0 \leq \sigma \leq 1$ is precomputed according to the local grid quality. Specifically, this parameter is calculated as [25]

$$\sigma = c\|D + D^T\| \qquad (2)$$

in which c is a constant value assigned as 0.2. D is the difference operator in the reconstruction process. For a uniform Cartesian grid, a skew-symmetric difference operator (i.e., $D = -D^T$) can be obtained when a polynomial interpolation is applied to reconstruct the left and right states of a certain control-volume face. Otherwise, a non-skew-symmetric difference operator can be obtained. The skew-symmetric property of the difference operator D provides a measurement of the reconstruction error. In the regions where local grid quality is perfect, the reconstruction error is small and the scheme reduces to a nondissipative central scheme ($\sigma = 0$). In the regions where local grid quality is not good, the reconstruction error is large and the upwind flux is added ($0 < \sigma \leq 1$) to prevent numerical instability. The method to calculate the blending parameter was first used on an unstructured solver [25]. It is applied on a structured code in this paper. The computation procedure of D can be found in [25].

Vreman's subgrid-scale model [31] is applied to calculate the subgrid eddy viscosity for modeling the effect of unresolved turbulent structures. The subgrid eddy viscosity can be expressed as

$$\nu_t = c\sqrt{\frac{B_\beta}{\alpha_{ij}\alpha_{ij}}} \qquad (3)$$

$$\alpha_{ij} = \frac{\partial u_j}{\partial x_i} \qquad (4)$$

$$B_\beta = \beta_{11}\beta_{22} - \beta_{12}^2 + \beta_{11}\beta_{33} - \beta_{13}^2 + \beta_{22}\beta_{33} - \beta_{23}^2 \qquad (5)$$

$$\beta_{ij} = \Delta_m^2 \alpha_{mi}\alpha_{mj} \qquad (6)$$

in which u_j is the filtered velocity, and Δ_m is the filter width. This model is easy to implement in LES because it only requires the local filter width and velocity derivatives.

In the WMLES method, the LES grid is designed to resolve only the large-scale eddies in the outer layer of the boundary layer. The velocity profile of the unresolved inner layer is computed using the equilibrium boundary-layer equations [32]:

$$\frac{\partial}{\partial y}\left[(\mu + \mu_t)\frac{\partial u}{\partial y}\right] = 0 \qquad (7)$$

$$\frac{\partial}{\partial y}\left[(\mu + \mu_t)u\frac{\partial u}{\partial y} + c_p\left(\frac{\mu}{Pr} + \frac{\mu_t}{Pr_t}\right)\frac{\partial T}{\partial y}\right] = 0 \qquad (8)$$

in which u is the resultant velocity parallel to the wall, T is the temperature, y is the wall-normal distance, μ is the dynamic viscosity, μ_t is the eddy viscosity, c_p is the specific heat at constant pressure, Pr is the laminar Prandtl number, and Pr_t is the turbulent Prandtl number. The eddy viscosity is taken from a mixing-length model, $\mu_t/\mu = \kappa y^+[1 - \exp(-y^+/A^+)]$ in which the Karman constant $\kappa = 0.41$ and $A^+ = 17$. A one-dimensional wall-model grid in the wall-normal direction is applied on each grid cell adjacent to the wall to solve the wall-model equations (7) and (8). For the wall-model grid, the boundary condition on the lower boundary $y = 0$ is an adiabatic no-slip condition. The wall-parallel velocity and temperature at the upper boundary of the wall-model grid are interpolated from the LES solution. After the velocity and temperature profiles are obtained from Eqs. (7) and (8), the shear stress and heat flux are obtained and applied as the wall boundary condition of the LES grid.

B. Problem Description

Two iced airfoils, the GLC305 airfoil with rime ice 212 [3] and the NLF0414 airfoil with glaze ice 623 [2], are studied in this paper. Both iced airfoils have horn features. The NLF0414/623 has two horns,

whereas the GLC305/212 has one inconspicuous horn. Figure 1 shows the geometries of the iced configurations. The black curves are the baseline airfoils, and the blue curves are the ice shapes. Experimental results for both configurations can be found in previous studies [2–4,27]. The full-scale ice-accretion experiments were conducted at the NASA John H. Glenn Research Center's Icing Research Tunnel. The 2-D ice shapes were made from the tracings of ice at a certain spanwise location, and then smoothed. Details of the ice shapes can be found in Ref. [4]. The 212 ice shape is the smoothed tracing at a 30% spanwise location of the 16.7 min ice accreted on the GLC305 airfoil. The 623 ice shape is the smoothed tracing at a 36% spanwise location of the 22.5 min ice accreted on the NLF0414 airfoil.

Figure 2 shows the computational grids of the iced airfoils and the regions near the horns. Every other grid line is plotted in the figure. The baseline topology of each grid is a C-type structured grid. The far-field boundaries are located 50 chord lengths (c) away from the airfoil to diminish the influence of the boundary condition. The spanwise domain size is $0.4c$. The effect of the spanwise domain size will be examined in the next section via a spanwise correlation analysis. The grid details are presented in Table 1 for the two configurations. N_x, N_y, and N_z are the numbers of grid points along the circumference direction, the wall-normal direction, and the spanwise direction, respectively. The total numbers of nodes are 15.92 million and 16.19 million for GLC305/212 and NLF0414/623, respectively, and the first layer heights are $1.1 \times 10^{-4}c$ and $1.5 \times 10^{-4}c$, respectively.

Figure 3 shows the distribution of the blending parameter σ in Eqs. (1) and (2) for the I-direction (along the circumference direction) and J-direction (wall-normal direction) cell faces of the grids shown
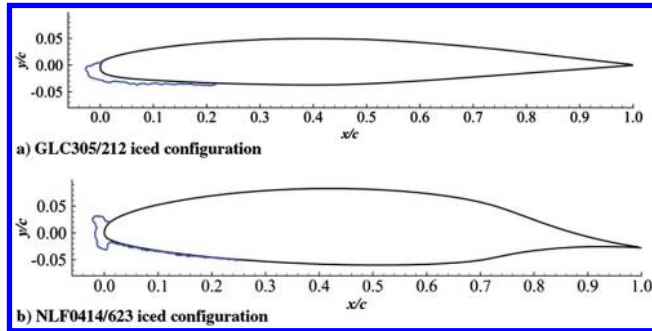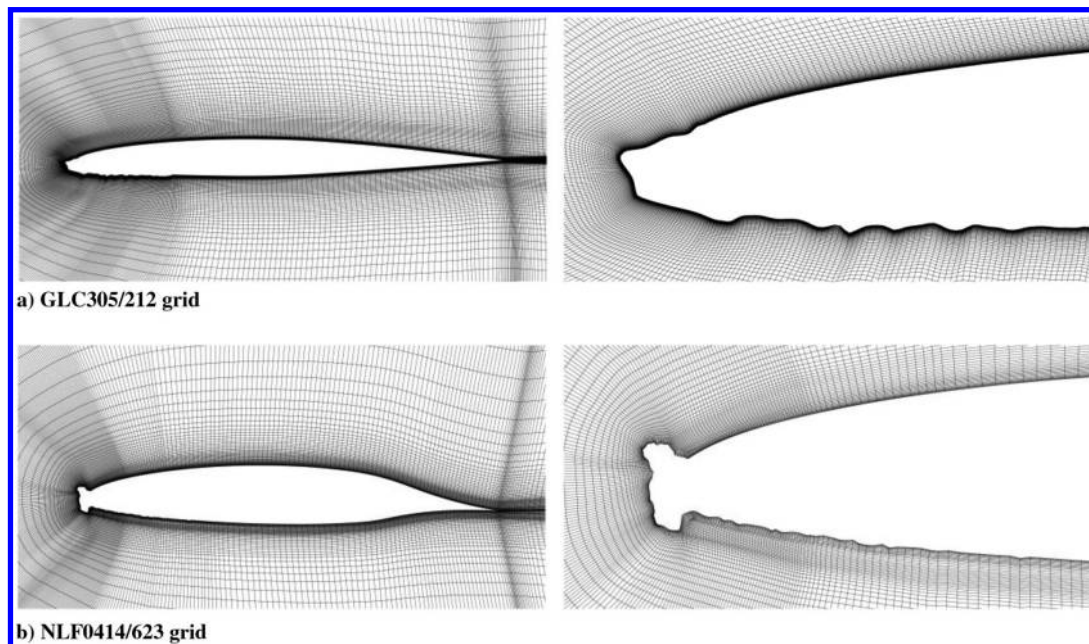
Table 1   Computational grid details

	N_x	N_y	N_z	Node number, million	First layer height ($\Delta y/c$)
GLC305/212	781	135	151	15.92	1.1×10^{-4}
NLF0414/623	831	121	161	16.19	1.5×10^{-4}

in Fig. 2. The contour range is (0, 0.3). The blending parameter σ is large in the region where grid orthogonality is poor or the space distribution is far from uniform. For both iced configurations, the grids near the ice accretions and the patch boundaries between grid blocks are relatively poor; consequently, the σ is relatively high.

Figure 4 shows the first grid layer height Δy^+ of the LES grid calculated from the wall friction velocity at 6 deg of the GLC305/212 configuration and 5.2 deg of the NLF0414/623 configuration. The results are collected after the LES computations. The Δy^+ is approximately 20.0–30.0 on most parts of the airfoils. The maximum values appear on the ice-horn tips, which are caused by the flow acceleration at the tips. On the lower surfaces, the jumps of Δy^+ before $x/c = 0.3$ are due to the rough surfaces of the ice accretions. The value of Δx^+ is approximately 180–200 for both configurations, and the value of Δz^+ is approximately twice the value of Δx^+.

In this paper, the one-dimensional grid for solving the wall-model equations covers three layers of the LES grid in the wall-normal direction to avoid a log-layer mismatch defect. The upper boundary of the wall-model grid is located at approximately $h_{wn}^+ = 75$, which satisfies the requirements of $h_{wn}^+ \geq 50$ and $h_{wn} < 0.1\delta$ suggested by Kawai and Larsson [32]. Sixty-one points are distributed in the wall-normal grid to solve Eqs. (7) and (8), and the first off-wall point is located at $\Delta y^+ < 1$ to capture the turbulent boundary layer.

C.   Grid-Convergence Study

To test the grid-convergence of LES computations, three grids with 5.87 million, 15.92 million, and 28.20 million points are used for the of the GLC305/212 simulation. The details of the medium grid have been presented in Table 1. The coarse and fine grids are obtained by reducing and increasing the node number of the medium grid by about 30% in all directions. Figure 5 compares the mean surface pressure coefficient at $Ma = 0.21$, AOA = 6.0 deg, and $Re = 7.5$ million with the experimental data [27]. The results show that the pressure distributions of the medium and fine grids agree well with the experimental values. The C_p values for the coarse and medium grids are almost the same except near the ice horn. The C_p
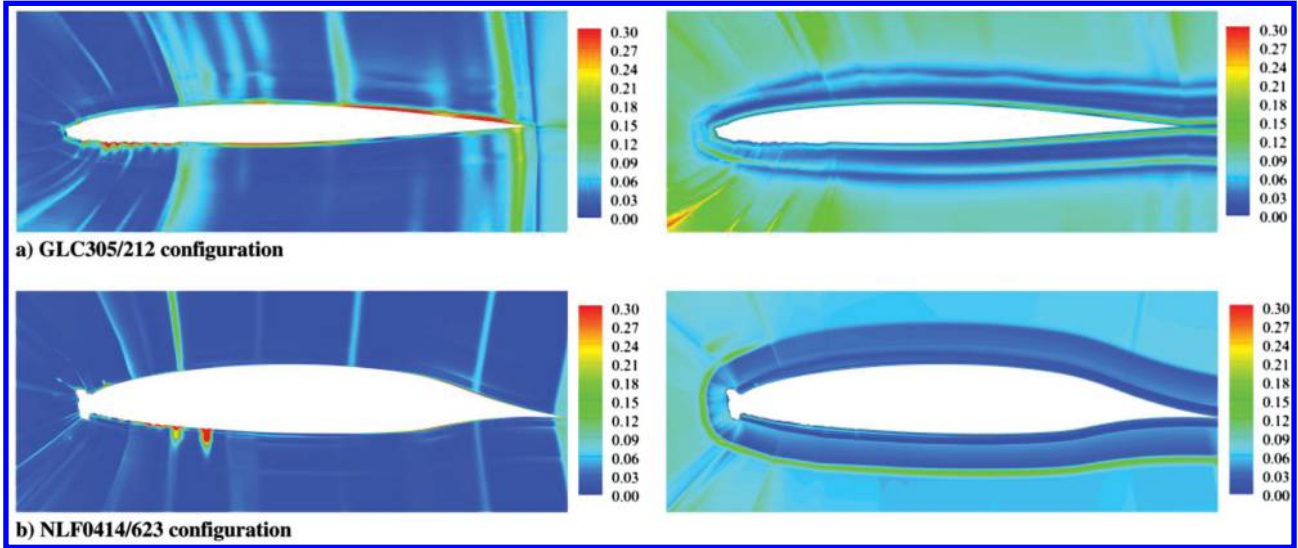

a) GLC305/212 iced configuration

b) NLF0414/623 iced configuration

Fig. 1   Geometries of the iced airfoils.

a) GLC305/212 grid

b) NLF0414/623 grid

Fig. 2   Computational grids around the iced airfoils (left) and near the ice horns (right).

Fig. 3 Distribution of blending parameter σ for the *I*-direction cell face (left) and *J*-direction cell face (right).
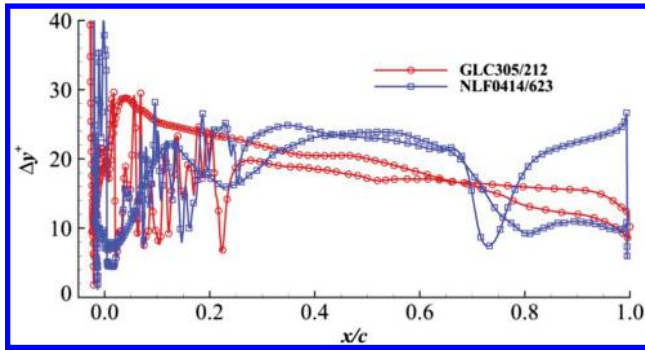

Fig. 4 First grid layer height Δy^+.

values for the medium and fine grids are similar. However, the fine grid predicts more pressure protuberances on the lower surface contaminated by ice accretions. Compared with the experimental data, the calculated pressure plateau after the ice horn is slightly shorter and the pressure recovery is slightly faster. The small discrepancy may be attributed to the wake blockage, potential probe support interference effects in the wind tunnel [27], or the grid resolution and numerical scheme in the computation. Because the medium grid predicts nearly the same result as the fine grid especially near the ice horn on the upper surface, the medium grid is used for other calculations in the following.

III. Numerical Results

In this section, the computational results for the GLC305/212 and NLF0414/623 configurations are presented. Table 2 shows the flow

conditions of the two configurations. First, statistical results, including lift coefficient, drag coefficient, pressure distribution, and mean flowfield, are studied. Then, instantaneous flowfields and pressure fluctuations are analyzed to investigate the unsteadiness. Finally, the characteristics of the shear layer and the reattachment are studied.

A. Statistical Results

The mean lift and drag coefficients at different AOA are shown in Fig. 6. Both LES and RANS results for the iced airfoils are presented. RANS results for the clean airfoils are also presented. In the RANS simulation, the total numbers of the 2-D grids are 60,000 and 40,000 for the GLC305/212 and the NLF0414/623, respectively. Menter's shear-stress-transport turbulence model [33] is employed to compute the eddy viscosity. The first layer grid height Δy^+ is less than 1.0 strictly to capture the turbulent boundary layer. Experimental data for both clean and iced airfoils are plotted for comparison [2–4,27]. Compared with the RANS, the LES method predicts the lift coefficients more accurately. The relative errors of the LES are less than 5% under all calculated conditions. Although the RANS can well predict the drag coefficients at low-lift conditions, it fails near stall. By contrast, the drag coefficients calculated from the LES agree much better with the experiments near and after stall.

Figure 6 also shows that the ice accretion decreases the maximum lift coefficient of the clean airfoil by approximately 40% and the stall angle by 2.0 deg for the GLC305/212 configuration, and it decreases the maximum lift coefficient by approximately 43% and the stall angle by 9.2 deg for the NLF0414/623 configuration. In addition, the ice accretion changes the stall behaviors of the two airfoils. The stall mode is changed from an abrupt loss of lift to a gradual loss of lift.
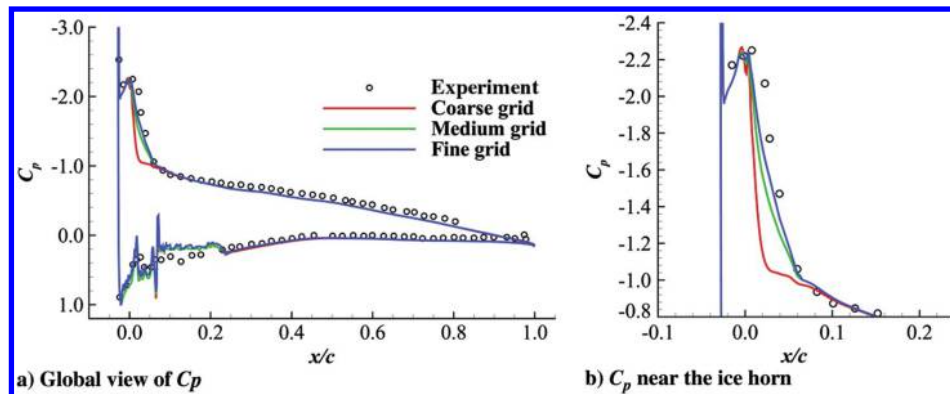

Fig. 5 Comparison of the mean surface pressure coefficient and experimental data.

Table 2   Flow conditions

	Mach number	Reynolds number, million	AOA, deg
GLC305/212	0.21	7.50	6.0, 8.0, 10.0, 12.0
NLF0414/623	0.21	4.60	3.0, 5.2, 7.0

The former stall mode is a leading-edge stall and the latter is a thin-airfoil stall. This change is attributed to the separation bubble aft of the ice shape. Although the rime ice 212 on the GLC305 airfoil is not large and its horn feature is inconspicuous, it also leads to severe aerodynamic degradations. The small ice shape is capable of changing the leading-edge shape of an airfoil and destroying the suction peak at the leading edge. According to Ref. [34], the more front loaded an airfoil is, the more sensitive it is to an ice accretion. Both the GLC305 and NLF0414 are front-loaded airfoils [4,27] with a strong suction peak at the leading edge at low speeds. Consequently, the ice accretion on these airfoils causes considerable aerodynamic degradations.

The mean surface pressure coefficients at different AOA for the two configurations are shown in Fig. 7. Because of the ice accretions, the suction peaks of the clean airfoils are replaced by plateaus. The locations of the pressure recovery start after the plateaus, which are inside the separation bubbles. Then, the pressure increases and the flow reattaches. The experimental data of the two iced configurations are also shown in the figure. The experimental Mach number and Reynolds number are slightly different from the present computation for the GLC305/212 configuration. However, according to Refs. [2,3], the effects of Reynolds number and Mach number on the pressure distribution are small for an iced airfoil with a leading-edge horn ice at low-speed conditions. Consequently, the experimental pressure coefficients are adopted to validate the present computation. Both the pressure coefficients of the GLC305/212 and NLF0414/623 match well with the experiment. The suction plateau after the ice horns and the pressure recovery after the separation bubble are well predicted by the present LES, which was not achieved with DES-type methods [17].

The streamlines of the mean flowfields are shown in Figs. 8 and 9 for the GLC305/212 and NLF0414/623 configurations, respectively. As the AOA increases, the separation-bubble length increases; consequently, the chordwise length of the pressure plateau increases and the pressure recovery starts later with a lower speed. In addition, the pressure at the trailing edge decreases for the iced airfoil when the AOA increases. This phenomenon was also observed in the experiment on a NACA 0012 airfoil with a leading-edge horn ice [5].

For the GLC305/212 configuration, the separation bubble takes up the full extent of the upper surface at 12 deg; thus, nearly constant pressure dominates the upper surface.

The separation bubble and reattachment location can be clearly seen in Figs. 8 and 9. The separation bubble is small and develops slowly before stall, whereas the bubble grows fast after stall. This phenomenon is also found in a previous study [35] at a high Reynolds number. For the NLF0414/623 configuration, the reattachment points are located at $0.16c$, $0.24c$, and $0.43c$ at 3.0, 5.2, and 7.0 deg, respectively, whereas for the GLC305/212 configuration, the reattachment locations are $0.09c$ and $0.38c$ at 8 and 10 deg, respectively. When the airfoil incidence increases to 12 deg, the
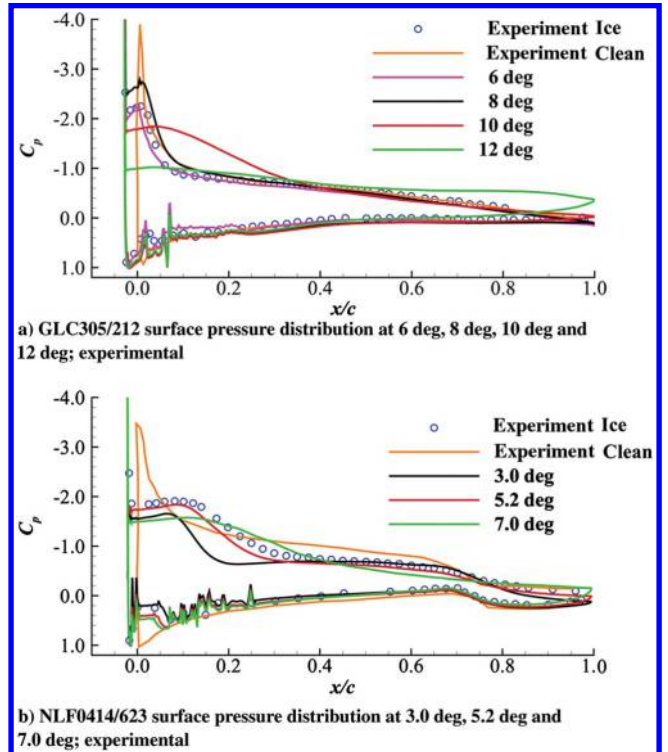

a) GLC305/212 surface pressure distribution at 6 deg, 8 deg, 10 deg and 12 deg; experimental

b) NLF0414/623 surface pressure distribution at 3.0 deg, 5.2 deg and 7.0 deg; experimental

Fig. 7   Distribution of calculated and experimental mean surface pressure coefficients.

a) GLC305/212 configuration
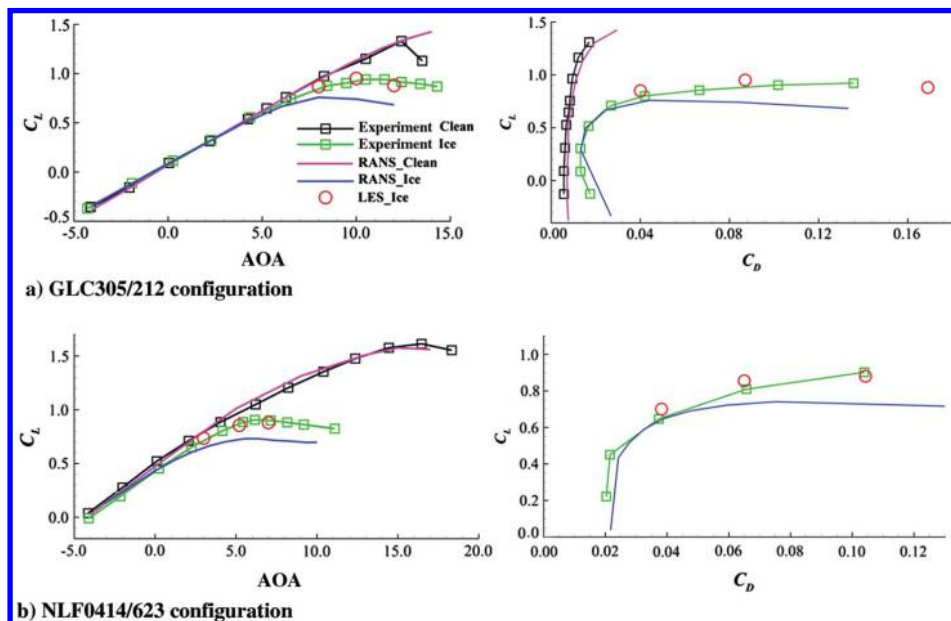
b) NLF0414/623 configuration

Fig. 6   Comparison of calculated mean lift (left) and drag (right) coefficients with experiments [2–4].
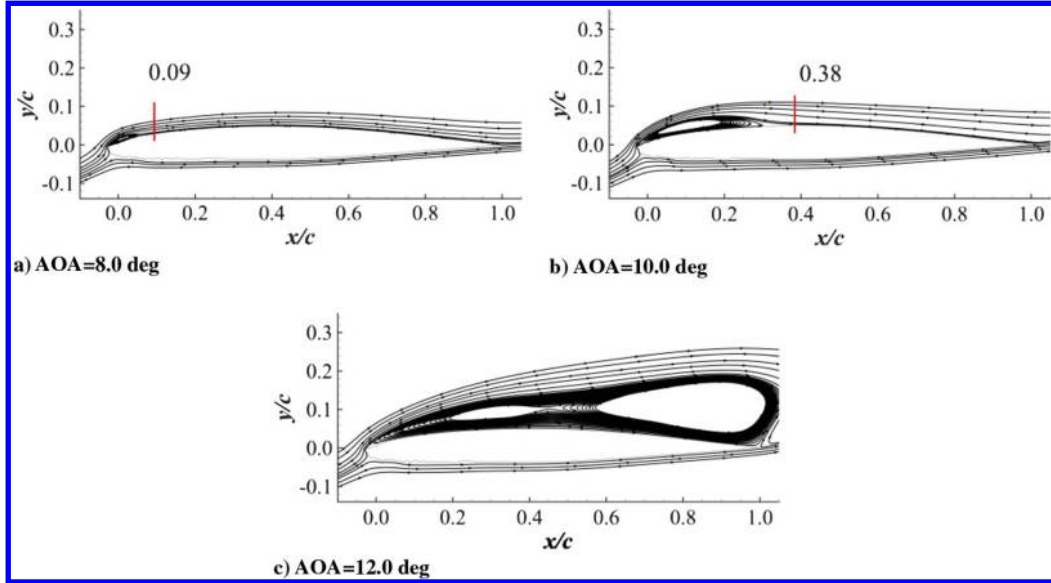
Fig. 8   Time-averaged streamlines at 3.0, 5.2, and 7.0 deg for the GLC305/212 configuration.
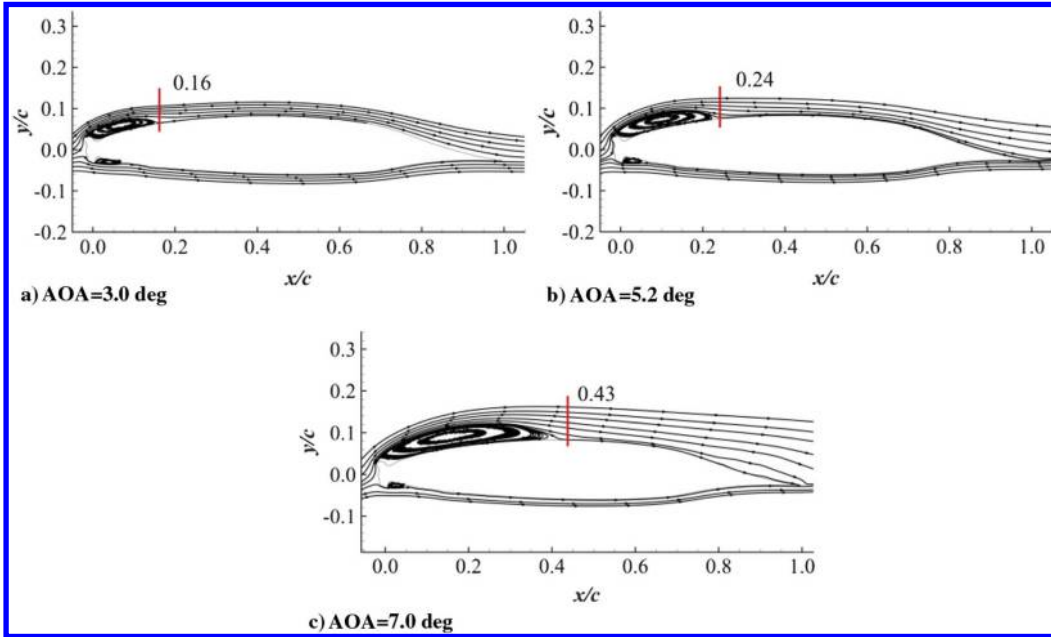

Fig. 9   Time-averaged streamlines at 3.0, 5.2, and 7.0 deg for the NLF0414/623 configuration.

separation bubble breaks up into two bubbles, and no obvious reattachment is observed. Marongiu et al. [35] claimed that the upper surface reattachment location of an iced airfoil grows as the square of the AOA. To determine the reattachment location, the relation between the reattachment location and the AOA for the NLF0414/ 623 configuration is curve fitted via the quadratic equation, $x_r/c = a\alpha^2 + b$, in which x_r/c is the reattachment location and α is the AOA in radians. Table 3 compares the reattachment location between the calculation results and the quadratic fitting results. The discrepancies are only $-0.015c$, $0.028c$, and $-0.012c$ for 3.0, 5.2, and 7.0 deg, respectively.

B.   Instantaneous Fields and Fluctuations

In this section, the instantaneous flowfield is analyzed to study the aerodynamic performance of an iced airfoil near stall. Figures 10 and 11 show the turbulent structures plotted by the Q criteria [36] for the GLC305/212 and NLF0414/623 configurations, respectively. The isosurface of $Q(c/U_\infty)^2 = 120$ is plotted and it is colored by

streamwise velocity u/U_∞. The flow structures are similar for both configurations. The free shear layer after the ice horn appears on the upper surface. Then, the shear layer K–H instability arises and spanwise eddy structures are formed. The spanwise eddies cannot maintain themselves and roll up into 3-D vortices. Then, the vortex structures become larger and more chaotic when spreading downstream. It should be noted that the DES-type method delays the

Table 3   Comparison of reattachment location between the calculation results and quadratic fitting for NLF0414/623

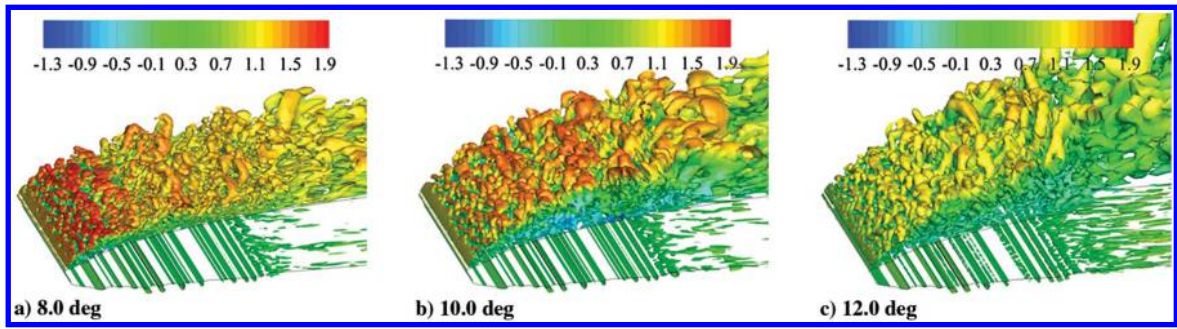|	AOA, deg		
	3.0	5.2	7.0
Calculation (x_r/c)	0.160	0.240	0.430
Quadratic fitting (x_r/c) ($a = 22.38$; $b = 0.0834$)	0.145	0.268	0.418
Error ($\Delta x_r/c$)	−0.015	0.028	−0.012

Fig. 10   Instantaneous turbulent eddy structures for the GLC305/212 airfoil.
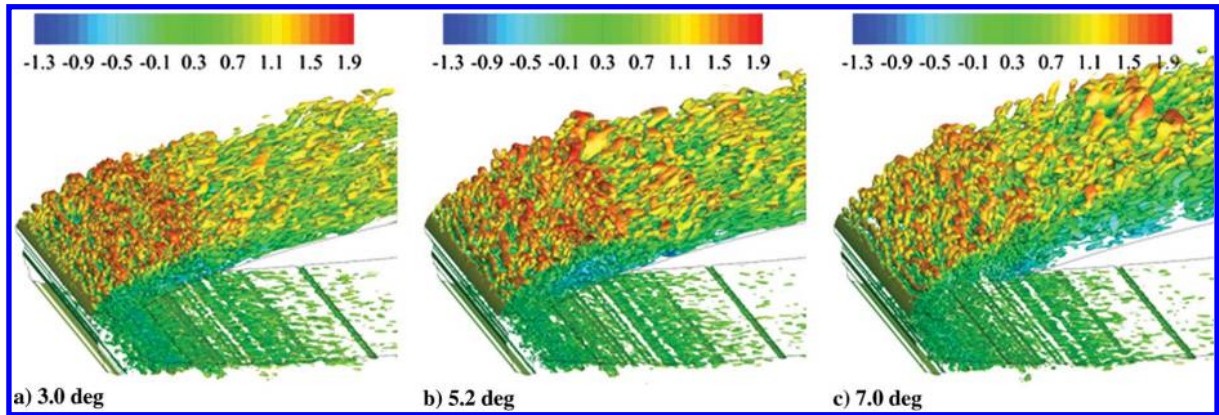

Fig. 11   Instantaneous turbulent eddy structures for the NLF0414/623 configuration.

K–H instability of the free shear layer, as shown in Refs. [13,18,20], because the DES-type method cannot resolve the small turbulent structures due to the large-eddy viscosity in the shear layer if the grid resolution is insufficient. By contrast, the present LES predicts the K–H instability reasonably. With the increase of airfoil incidence, turbulent structures become abundant on the upper surface. At the same time, more vortices convect downstream and the scale of the turbulent structures becomes larger. Although the horn feature of rime ice 212 is not obvious, it also induces strong unsteady turbulent structures (Fig. 10). This phenomenon significantly changes the flow acceleration at the leading edge of a clean airfoil.

Because of the existence of a small ice horn on the lower surface of the NLF0414/623 configuration, the 3-D vortices are also induced near the leading edge of the lower surface (Fig. 11). Fortunately, ice accreted on the lower surface has no significant impact on the stall behavior, although it causes a change of drag and moment coefficients at low and negative AOA [37].

To further demonstrate the flow features aft of the ice horn, the instantaneous spanwise vorticities at $z/c = 0.2$ are shown in Fig. 12. The vortices in the shear layer roll up due to strong adverse pressure gradients, and enhance mixing of the low-energy separated flow and the high-energy main flow. This phenomenon shows that the LES method can effectively predict the strong vortex shedding and roll-up pattern just aft of the ice horn. The curves in Fig. 12 are the time-averaged streamlines. With an increased AOA, the vortices move further upward and downstream. For the GLC305/212 configuration, the turbulent structures are close to the surface at 8 and 10 deg, and the flow becomes reattached downstream. However, the recirculation takes up the entire upper surface and the separation bubble breaks up without reattachment at 12 deg. For the NLF0414/623 configuration, reattachment always occurs from 3.0 to 7.0 deg, while the vorticity distribution varies with time, and this variation directly influences the surface pressure distribution.

Figure 13 shows the rms contours of the pressure coefficient at 3.0, 5.2, and 7.0 deg for the NLF0414/623 configuration. In general, the maximum fluctuation occurs in the shear layer. As the AOA increases, the region of strong fluctuation enlarges significantly. However, this is not the case for the maximum fluctuation values, which are 0.30, 0.43, and 0.41 for 3.0, 5.2, and 7.0 deg, respectively. Figure 14 shows the distribution of $C_{p,\text{rms}}$ along eight lines, as shown in Fig. 13c for the NLF0414/623 configuration. The maximum fluctuation value decreases and the vertical spatial range of strong fluctuation increases as the air flows downstream. At $x/c = 1.0$, the fluctuation of pressure is near a constant value in the vertical direction at a certain AOA due to the strong mixing effect of turbulence. In addition, the mixing and dissipation of turbulence depress the maximum fluctuation. At a chordwise location before $x/c = 0.2$, the maximum fluctuation occurs at 5.2 deg, whereas it appears at 7.0 deg after $x/c = 0.2$ because more large turbulent structures develop downstream. In addition, the region of strong fluctuation moves upward and its vertical spatial range enlarges with increasing angle of incidence.

The rms of the wall pressure coefficient for the NLF0414/623 configuration is shown in Fig. 15. The numbers with arrows denote the reattachment locations. The pressure fluctuations of the clean airfoil are weak and do not vary with the AOA when the incidence is not high [38]. By contrast, an iced airfoil has a large region with strong fluctuations due to the flow separation. When the AOA increases from 3.0 to 5.2 deg, the peak value of the $C_{p,\text{rms}}$ increases from 0.158 to 0.165; then, the peak value decreases at 7.0 deg. The peak location of the $C_{p,\text{rms}}$ moves downstream when the AOA increases. In the experiment with the NACA 0012 airfoil with 3.5 min ice accretion [38], the peak value of the $C_{p,\text{rms}}$ increases until 8.0 deg when the separation bubble extends over the entire upper surface, after which the $C_{p,\text{rms}}$ decreases. However, the phenomenon in the present situation is slightly different. The reattachment point of the NLF0414/623 configuration is located at $43\%c$ at 7.0 deg. The decrease agrees with the reduction of the maximum flowfield
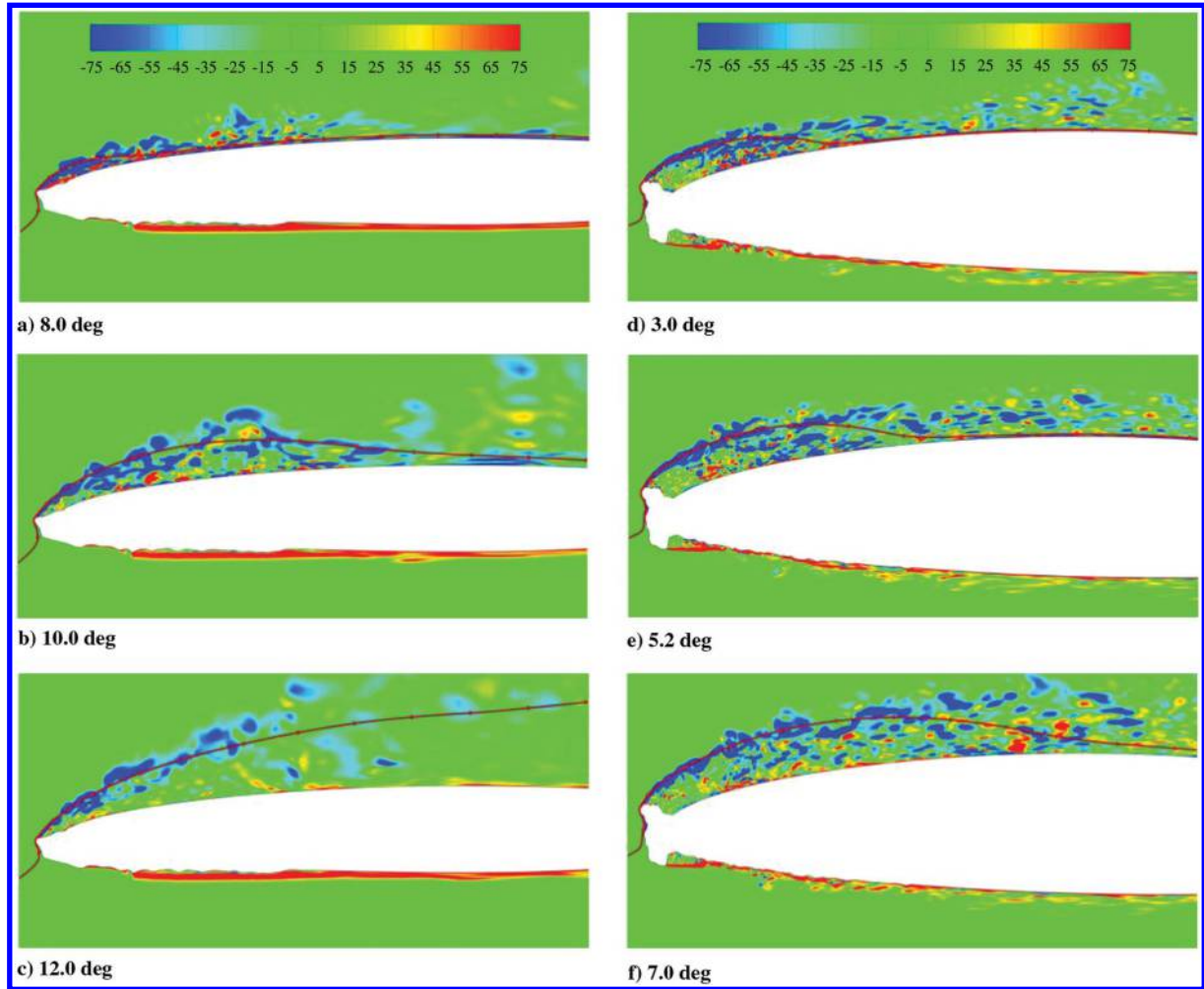
Fig. 12   Spanwise vorticity $\Omega_z (c/U_\infty)$ at different AOA for the GLC305/212 (left) and the NLF0414/623 (right).
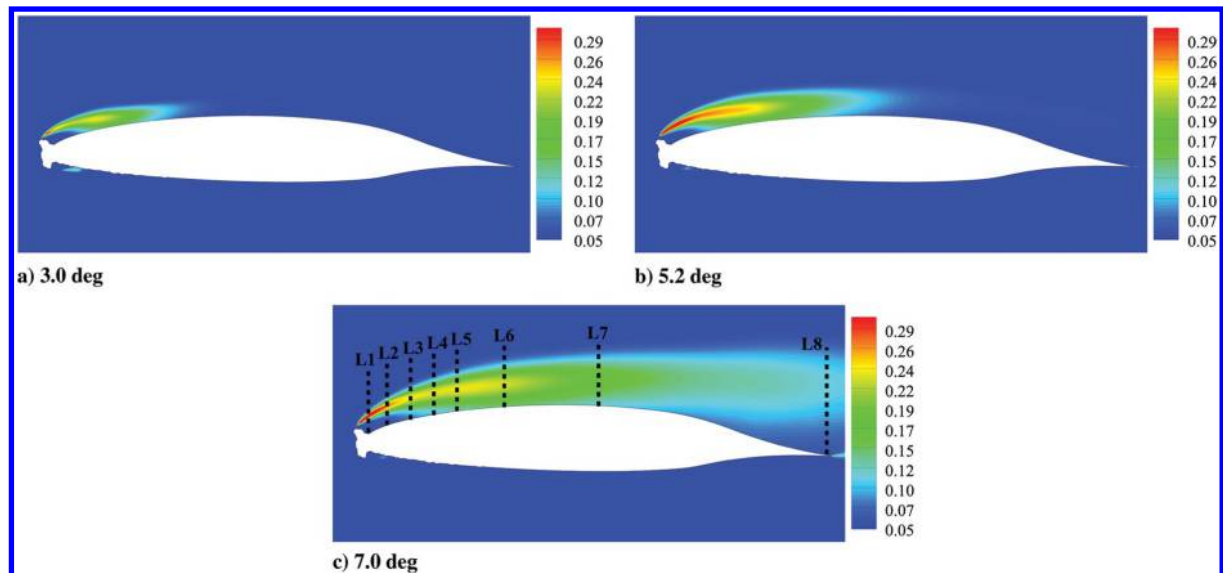

Fig. 13   RMS of pressure coefficient $C_{p,\mathrm{rms}}$ at 3.0, 5.2, and 7.0 deg.

pressure fluctuation from 5.2 to 7.0 deg, as shown in Fig. 13. In addition, the decrease of pressure fluctuation may be attributed to the elevation of the free shear layer and the unsteady turbulent structures shedding from the ice horn, which weakens the pressure fluctuations. Notably, the reattachment occurs aft of the location of the peak $C_{p,\mathrm{rms}}$.

This pattern is consistent with the fact that the turbulent structures gradually decay after the reattachment.

Table 4 lists the rms of the lift coefficient for both configurations. The fluctuation amplitude is small at low AOA and increases rapidly at high AOA. This pattern is consistent with the change of the
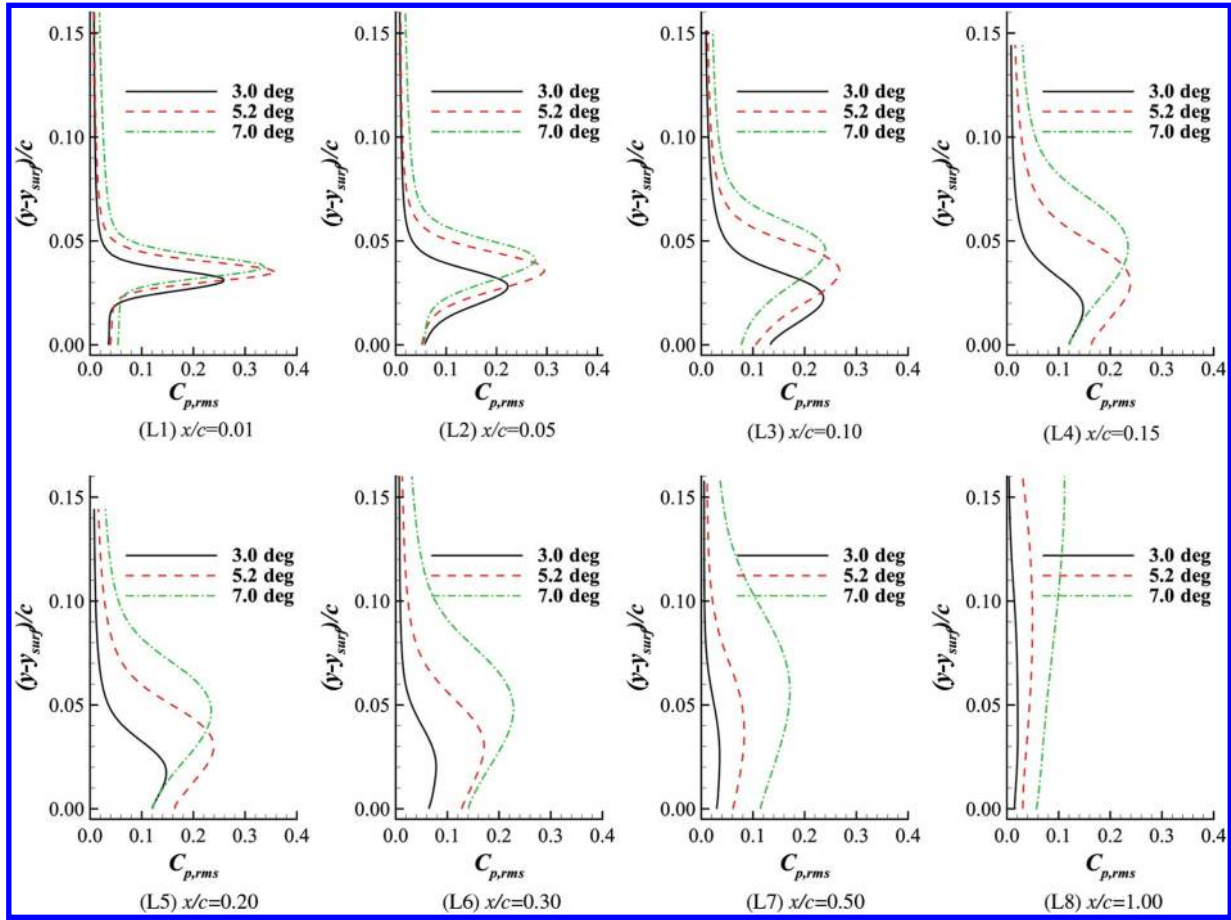
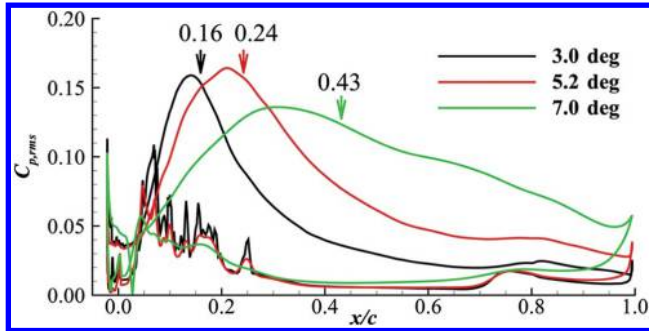Fig. 14   Distribution of $C_{p,\mathrm{rms}}$ along eight lines shown in Fig. 13c.

Fig. 15   RMS of surface pressure coefficient at 3.0, 5.2, and 7.0 deg.

Fig. 16   Mean spanwise vorticity $\Omega_z (c/U_\infty)$ and eight probe locations.

separation bubble analyzed in the previous section, whose length increases as the square of the AOA. The lift displays strong unsteadiness after stall.

C. Spectrum Analysis of the Pressure Fluctuation

Strong unsteadiness exists in the flowfield of an iced airfoil. K–H instability and vortex shedding from the ice horn induce unsteady
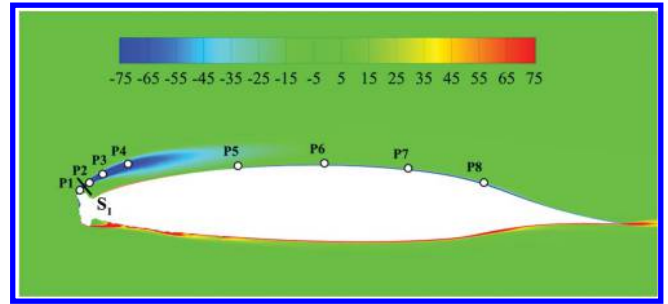
turbulent structures. In this section, the fast Fourier transform method is used to investigate the pressure fluctuations of the NLF0414/623 iced configuration.

Figure 16 shows the contour of the mean spanwise vorticity and eight locations of pressure probes for the NLF0414/623 configuration at 5.2 deg. Points P_1 to P_4 are located in the free shear layer. Points P_5 to P_8 are placed on the upper surface. Figure 17 shows the spanwise correlations of the pressure fluctuations at four probes: P_2, P_4, P_5, and P_7. The maximum distance of the correlation is half of the spanwise computational domain size. The correlation between points at z and $z + \Delta z$ is calculated as [39]

$$R(\Delta z) = \frac{\overline{p'(z)p'(z + \Delta z)}}{\sqrt{\overline{p'(z)^2}}\sqrt{\overline{p'(z + \Delta z)^2}}} \tag{9}$$

As shown in Fig. 17, the correlations decay rapidly for P_2 and P_4 due to the small sizes of the eddy structures in the mixing shear layer. The correlations decay to nearly 0.0 at $z/c = 0.1$. The correlations of

Table 4   RMS of lift coefficient at different AOA for GLC305/212 and NLF0414/623 configurations

GLC305/212		Nlf0414/623	
AOA, deg	$C_{L,\mathrm{rms}}$	AOA, deg	$C_{L,\mathrm{rms}}$
8.0	0.0029	3.0	0.0028
10.0	0.0267	5.2	0.0087
12.0	0.1576	7.0	0.0291
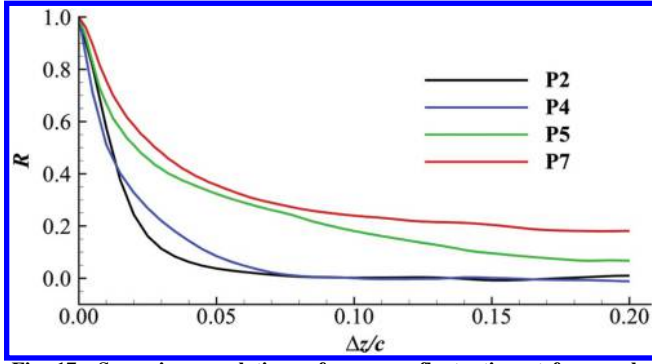
Fig. 17 Spanwise correlations of pressure fluctuation at four probe locations—P_2, P_4, P_5, and P_7.

Fig. 20 Distribution of velocity magnitude along the line S_1 in Fig. 16 from bottom to top.

P_5 and P_7 decay more slowly than those of P_2 and P_4. The P_7 decays slowly to approximately 0.2 at $z/c = 0.2$, which may be caused by the large vortex size after reattachment. However, this point is far from the separation bubble and has no significant effect on the mixing shear layer and the reattachment. Consequently, the correlation results demonstrate that the spanwise length of $0.4c$ is sufficient in the present computation.

Figure 18 shows the PSD of the pressure fluctuations at four points —P_1 to P_4—in the free mixing shear layer for NLF0414/623 at 5.2 deg. The spectrum of P_1 has one strong peak $f_1 c/U_\infty = 55.92$, and P_4 has one peak $f_2 c/U_\infty = 28.81$. Both P_2 and P_3 show two peaks f_1 and f_2. The high-frequency peak corresponds to the initial vortex development in the shear layer caused by the K–H instability. The low-frequency peak is also caused by the vortex shedding in the
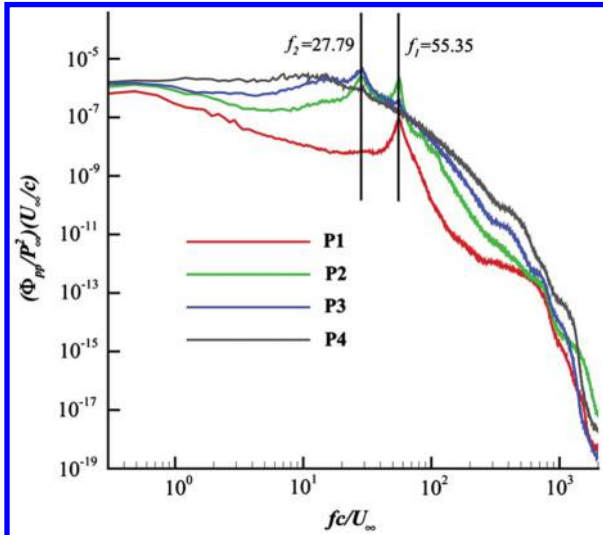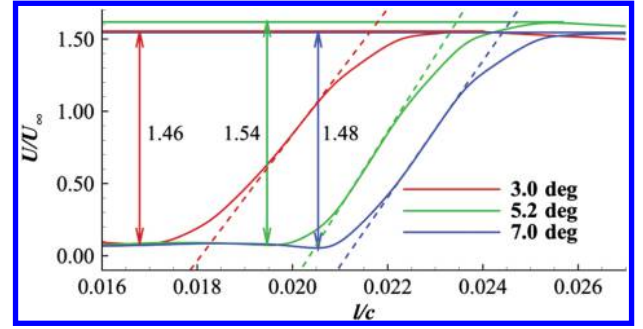
further downstream region of the shear layer. The decrease of characteristic frequency from 55.92 to 28.81 might be attributed to the merging of vortices. Figure 19 shows the instantaneous pressure coefficient fluctuations ($C_p - \overline{C_p}$) at three moments in the free mixing shear layer for the NLF0414/623 configuration at 5.2 deg. The time interval between two moments is $\Delta t U_\infty/c = 0.025$. From $t = t_0$ to $t = t_2$, vortices move downstream gradually, and two small vortices merge into a large one.

For the high-frequency f_1, following the definition of Duclercq et al. [19], the Strouhal number is defined by

$$St = \frac{f_1 \delta_w}{\Delta U} \quad (10)$$

in which ΔU is the velocity difference between the two mixing flows of the shear layer, and δ_w is the vorticity thickness computed by $\delta_w = \Delta U / \max(\partial U/\partial y)$. Figure 20 shows the distribution of velocity magnitude along the line S_1 in Fig. 16 from bottom to top. The velocity differences $\Delta U/U_\infty$ across the shear layer are 1.46, 1.54, and 1.48, and the corresponding vorticity thicknesses δ_w/c are 0.0033, 0.0030, and 0.0031 for 3.0, 5.2, and 7.0 deg, respectively. The three dashed lines in Fig. 20 show the maximum velocity gradient $\partial U/\partial y$ at three AOA. The calculated St_δ values at the three AOA are 0.152, 0.110, and 0.109, which are all near 0.135, the linear-stability-analysis value of a 2-D mixing layer [19].

Figure 21 shows the PSD of pressure fluctuations at three AOA at four probe locations P_1 to P_4 in the free shear layer for the NLF0414/623. In general, the spectra at three different AOA have similar patterns. Both high- and low-frequency peaks exist at all three AOA, although the frequency values are slightly different. Table 5 lists the two characteristic frequencies at three AOA for probe points P_1 to P_4. As the AOA increases, both high and low characteristic frequencies decrease. In addition, the two frequencies appear at P_1 and P_2 at 3.0 deg, whereas they appear at P_2 and P_3 for two higher angles. This is reasonable, because vortex shedding at low AOA reattaches to the surface more quickly. Thus, the vortices do not flow past points P_3 and P_4.

Figure 22 shows the PSD of pressure fluctuations at four points —P_5 to P_8—near and after reattachment for NLF0414/623 at 5.2 deg. The slope of the dashed line is $-5/3$. The spectra of the pressure fluctuation fit the $-5/3$ law quite well in the inertial

Fig. 18 PSD of pressure fluctuations at four probes—P_1 to P_4—in the free mixing shear layer.

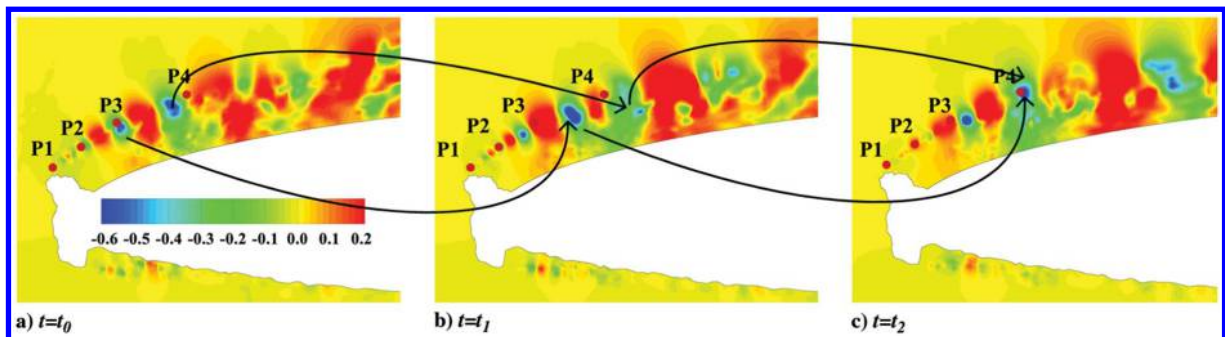Fig. 19 Contours of instantaneous pressure coefficient fluctuations ($C_p - \overline{C_p}$).
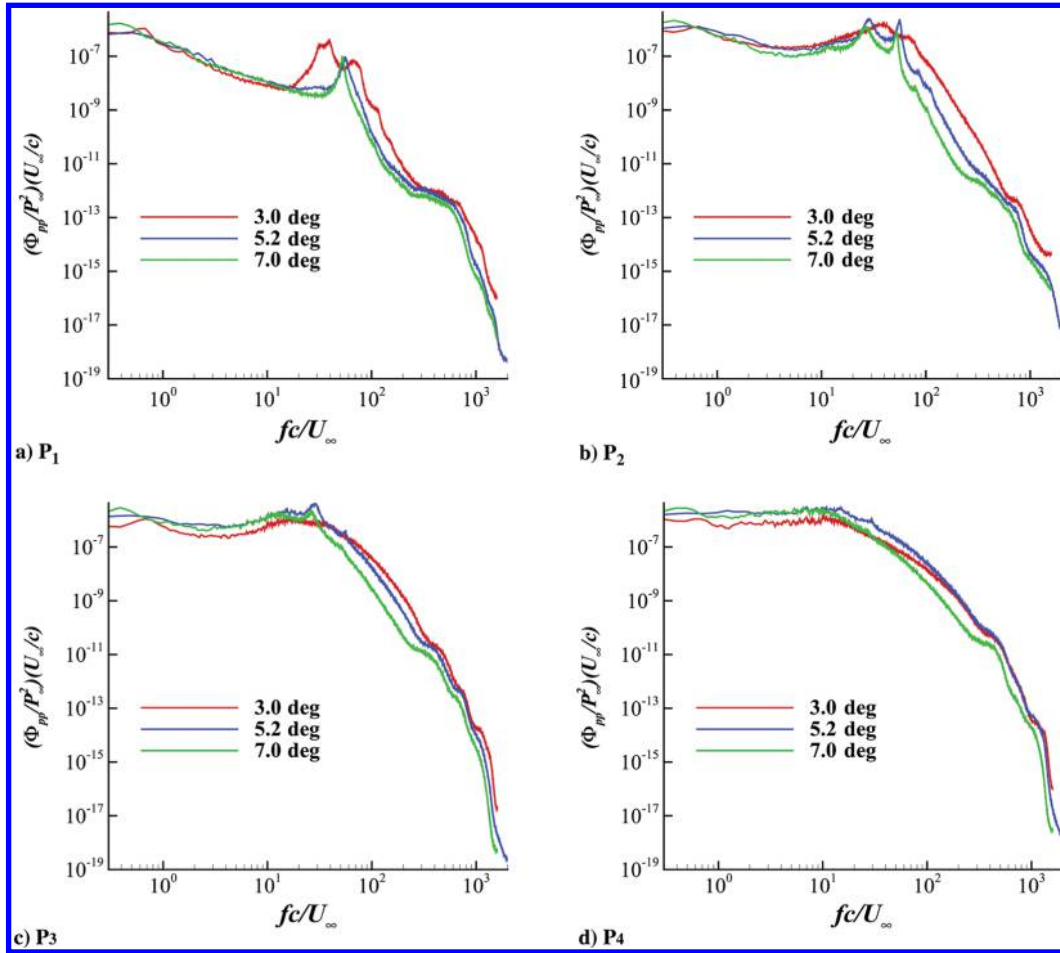
Fig. 21   PSD of pressure fluctuations at four probe locations—P_1 to P_4.

subrange, which demonstrates that the turbulence near the re-attachment has fully developed and has been well resolved by the present LES method. In particular, the dissipation introduced by the subgrid-scale model and the hybrid numerical central/upwind flux is appropriate. The spectra show a weak peak of $fc/U_\infty = 3.13$, which corresponds to a nondimensional St 0.75 based on the separation-bubble length and the freestream velocity. This frequency is attributed to both the vertical motion of the free shear layer and the shedding of the vortices into the flow downstream. Table 6 lists the Strouhal number found in the experiments on iced airfoils [40]. The present calculated Strouhal number is near the ranges of the experiments. However, the frequency peak, $fc/U_\infty = 3.13$, is weak, and several other weak peaks also exist. The experiment of Ansell and Bragg [41] on a NACA 0012 airfoil with a 3.5 min horn ice also illustrated that there is not an obvious discrete frequency near the reattachment [42,43].

Figure 23 shows the PSD of pressure fluctuations at three AOA for P_5 to P_8 on the upper surface near and after the reattachment for NLF0414/623. The slopes of the dashed lines are $-5/3$. All spectra fit the $-5/3$ law well in the inertial subrange. With the increasing
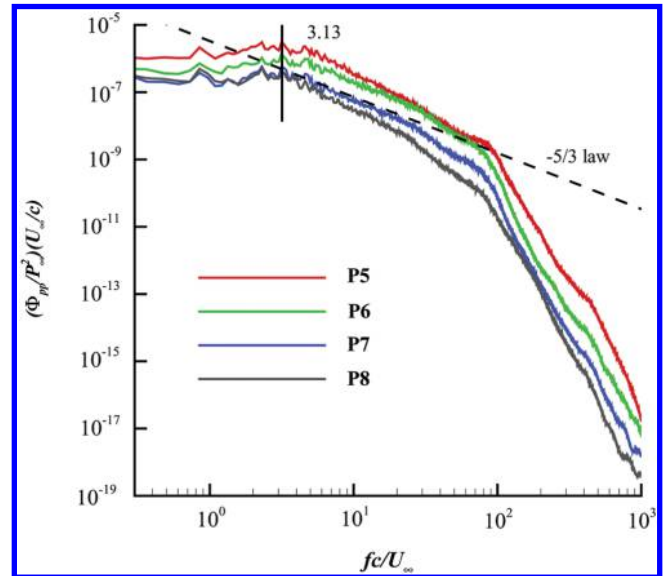

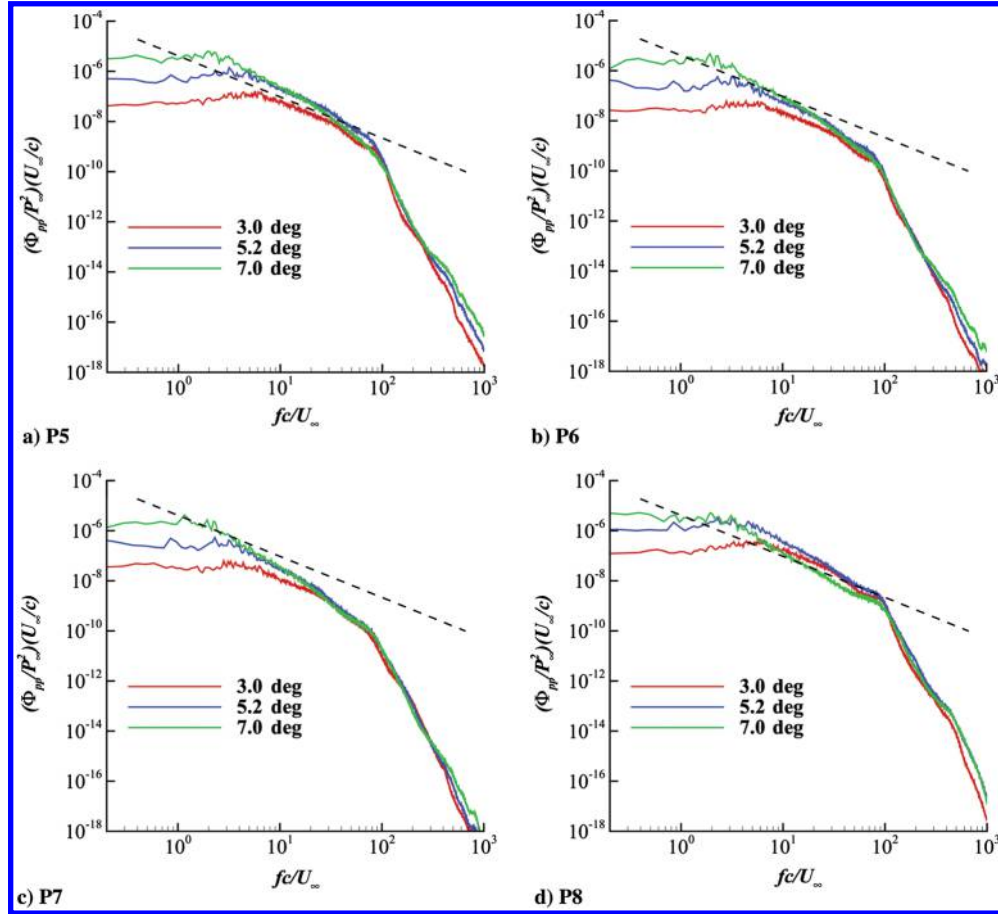**Fig. 22   PSD of pressure fluctuations at four probe locations—P_5 to P_8.**

AOA, low-frequency components increase because large-scale turbulent structures develop at larger AOA. Additionally, several inconspicuous frequency peaks exist between $fc/U_\infty = 0.8$ and $fc/U_\infty = 4.0$ at 3.0 and 7.0 deg as 5.2 deg and there is not a discrete frequency. This phenomenon demonstrates that the regular mode of vortex shedding is not frequency dominant near the reattachment.

Table 5   Two characteristic frequencies (fc/U_∞) at probes P_1 to P_4 at three AOA for the NLF0414/623 configuration

	P_1		P_2		P_3		P_4	
Angle, deg	Low	High	Low	High	Low	High	Low	High
3.0	38.73	67.40	38.78	67.59	——	——	——	——
5.2	——	55.92	28.81	55.92	28.81	55.44	28.81	——
7.0	——	51.85	26.53	52.58	26.53	52.68	——	——

Table 6   Comparison of Strouhal number for the regular mode of vortex [40]

Authors	Geometry	Reynolds number	Strouhal number
Current study	NLF0414 airfoil (with 2-D horn-ice shape)	4.6×10^6	0.75
Manshadi and Esfeh [40]	NACA 0015 airfoil (with 2-D horn-ice shape)	1.0×10^6	0.5–0.63
Gurbacki and Bragg [42]	NACA 0012 airfoil (with 2-D and 3-D horn-ice shape)	1.0×10^6 to 1.8×10^6	0.53–0.73
Mirzaei et al. [43]	NLF0414 airfoil (with 2-D horn-ice shape)	0.5×10^6	0.44–0.78

Fig. 23   PSD of pressure fluctuations at four probe locations—P_5 to P_8.

IV. Conclusions

The flow characteristics around two iced airfoils, GLC305/212 and NLF0414/623, were studied using an large-eddy simulation (LES) method. A combined central/upwind scheme was adopted to reduce the numerical dissipation and resolve more physical turbulent structures. Notably, the blending parameter only depended on the local grid quality. The close agreement of the calculated lift, drag, and surface pressure distribution with the experimental results illustrates that the present LES method is capable of accurately predicting the separated flow around iced airfoils, especially the K–H instability of the free shear layer, which is often delayed by DES-type methods. Specifically, the effect of airfoil incidence on the flow characteristics of iced airfoils was investigated.

With the increase of angle of attack (AOA), the separation bubble extended slowly before stall, whereas it grew fast after stall. For the NLF0414/623, the chordwise reattachment location increased with the AOA according to a quadratic relation. Maximum $C_{p,\text{rms}}$ always appeared just before the reattachment. Furthermore, it first increased, and then decreased as the AOA increased.

A high-frequency peak, $f_1 c/U_\infty = 55.92$, and a low-frequency peak, $f_2 c/U_\infty = 28.81$, were found at 5.2 deg for the NLF0414/623 configuration in the initial and further downstream regions of the free shear layer, respectively. The high frequency was caused by the K–H

instability and vortex shedding. The low frequency might be caused by the vortex merging. As the AOA increased, both characteristic frequencies decreased a bit. In addition, there was not a single-frequency peak near and after the reattachment for the NLF0414/623 configuration.

Notably, both configurations calculated in this paper were 2-D simplified ice shapes. The spanwise variations of ice shape were not considered. In the future, a more in-depth analysis to unsteady contents and modes in the flowfield of an iced airfoil will be performed.

Acknowledgments

References

[1] Lynch, F. T., and Khodadoust, A., "Effects of Ice Accretions on Aircraft Aerodynamics," *Progress in Aerospace Sciences*, Vol. 37, No. 8, 2001, pp. 669–767.
doi:10.1016/S0376-0421(01)00018-5

[2] Addy, H., and Chung, J., "A Wind Tunnel Study of Icing Effects on a Natural Laminar Flow Airfoil," *38th Aerospace Sciences Meeting and Exhibit*, AIAA Paper 2000-0095, Jan. 2000.
doi:10.2514/6.2000-95

[3] Addy, H., Broeren, A., Zoeckler, J., and Lee, S., "A Wind Tunnel Study of Icing Effects on a Business Jet Airfoil," *41st Aerospace Sciences Meeting and Exhibit*, AIAA Paper 2003-0727, Feb. 2003.
doi:10.2514/6.2003-727

[4] Addy, H., "Ice Accretions and Icing Effects for Modern Airfoils," NASA TP-2000-210031, 2000.

[5] Gurbacki, H. M., and Bragg, M. B., "Unsteady Aerodynamic Measurements on an Iced Airfoil," *40th AIAA Aerospace Sciences Meeting and Exhibit*, AIAA Paper 2002-0241, Jan. 2002.
doi:10.2514/6.2002-241

[6] Jacobs, J., and Bragg, M., "Particle Image Velocimetry Measurements of the Separation Bubble on an Iced Airfoil," *24th AIAA Applied Aerodynamics Conference*, AIAA Paper 2006-3646, June 2006.
doi:10.2514/6.2006-3646

[7] Ansell, P. J., and Bragg, M. B., "Unsteady Modes in Flowfield About Airfoil with Horn-Ice Shape," *Journal of Aircraft*, Vol. 53, No. 2, 2016, pp. 475–486.
doi:10.2514/1.C033421

[8] Bragg, M. B., Broeren, A. P., and Blumenthal, L. A., "Iced-Airfoil Aerodynamics," *Progress in Aerospace Sciences*, Vol. 41, No. 5, 2005, pp. 323–362.
doi:10.1016/j.paerosci.2005.07.001

[9] Cao, Y., Chen, K., and Sheridan, J., "Flowfield Simulation and Aerodynamic Performance Analysis of Complex Iced Aerofoils with Hybrid Multi-Block Grid," *Proceedings of the Institution of Mechanical Engineers, Part G: Journal of Aerospace Engineering*, Vol. 222, No. 3, 2008, pp. 417–422.
doi:10.1243/09544100JAERO286

[10] Chung, J., and Addy, H., "A Numerical Evaluation of Icing Effects on a Natural Laminar Flow Airfoil," *38th Aerospace Sciences Meeting and Exhibit*, AIAA Paper 2000-0096, Jan. 2000.
doi:10.2514/6.2000-96

[11] Pan, J., and Loth, E., "Reynolds-Averaged Navier-Stokes Simulations of Airfoils and Wings with Ice Shapes," *Journal of Aircraft*, Vol. 41, No. 4, 2004, pp. 879–891.
doi:10.2514/1.587

[12] Brown, C. M., Kunz, R. F., Kinzel, M. P., and Lindau, J., "Large Eddy Simulation of Airfoil Ice Accretion Aerodynamics," *6th AIAA Atmospheric and Space Environments Conference*, AIAA Paper 2014-2203, June 2014.
doi:10.2514/6.2014-2203

[13] Pan, J., and Loth, E., "Detached Eddy Simulations for Airfoil with Ice Shapes," *42nd AIAA Aerospace Sciences Meeting and Exhibit*, AIAA Paper 2004-0564, Jan. 2004.
doi:10.2514/6.2004-564

[14] Lorenzo, A., Valero, E., and Depablo, V., "DES/DDES Post-Stall Study with Iced Airfoil," *49th AIAA Aerospace Sciences Meeting Including the New Horizons Forum and Aerospace Exposition*, AIAA Paper 2011-1103, Jan. 2011.
doi:10.2514/6.2011-1103

[15] Mogili, P., Thompson, D., Choo, Y., and Addy, H., "RANS and DES Computations for a Wing with Ice Accretion," *43rd AIAA Aerospace Sciences Meeting and Exhibit*, AIAA Paper 2005-1372, Jan. 2005.
doi:10.2514/6.2005-1372

[16] Choo, Y. K., Thompson, D., and Mogili, P., "Detached-Eddy Simulations of Separated Flow Around Wings with Ice Accretions: Year One Report," NASA CR-2004-213379, 2004.

[17] Alam, M. F., Thompson, D. S., and Walters, D. K., "Hybrid Reynolds-Averaged Navier–Stokes/Large-Eddy Simulation Models for Flow Around an Iced Wing," *Journal of Aircraft*, Vol. 52, No. 1, 2015, pp. 244–256.
doi:10.2514/1.C032678

[18] Xiao, M., Zhang, Y., and Chen, H., "Numerical Study of an Iced Airfoil Using Window-Embedded RANS/LES Hybrid Method," *9th AIAA Atmospheric and Space Environments Conference*, AIAA Paper 2017-3761, June 2017.
doi:10.2514/6.2017-3761

[19] Duclercq, M., Brunet, V., and Moens, F., "Physical Analysis of the Separated Flow Around an Iced Airfoil Based on ZDES Simulations," *4th AIAA Atmospheric and Space Environments Conference*, AIAA Paper 2012-2798, June 2012.
doi:10.2514/6.2012-2798

[20] Zhang, Y., Habashi, W. G., and Khurram, R. A., "Zonal Detached-Eddy Simulation of Turbulent Unsteady Flow over Iced Airfoils," *Journal of Aircraft*, Vol. 53, No. 1, 2016, pp. 168–181.
doi:10.2514/1.C033253

[21] Xiao, Z., Liu, J., Huang, J., and Fu, S., "Numerical Dissipation Effects on Massive Separation Around Tandem Cylinders," *AIAA Journal*, Vol. 50, No. 5, 2012, pp. 1119–1136.
doi:10.2514/1.J051299

[22] Bui, T. T., "A Parallel, Finite-Volume Algorithm for Large-Eddy Simulation of Turbulent Flows," *Computers & Fluids*, Vol. 29, No. 8, 2000, pp. 877–915.
doi:10.1016/S0045-7930(99)00040-7

[23] Shur, M. L., Spalart, P. R., Strelets, M. K., and Travin, A. K., "Towards the Prediction of Noise from Jet Engines," *International Journal of Heat and Fluid Flow*, Vol. 24, No. 4, 2003, pp. 551–561.
doi:10.1016/S0142-727X(03)00049-3

[24] Strelets, M., "Detached Eddy Simulation of Massively Separated Flows," *39th Aerospace Sciences Meeting and Exhibit*, AIAA Paper 2001-0879, July 2001.
doi:10.2514/6.2001-879

[25] Khalighi, Y., Ham, F., Nichols, J., Lele, S., and Moin, P., "Unstructured Large Eddy Simulation for Prediction of Noise Issued from Turbulent Jets in Various Configurations," *17th AIAA/CEAS Aeroacoustics Conference (32nd AIAA Aeroacoustics Conference)*, AIAA Paper 2011-2886, June 2011.
doi:10.2514/6.2011-2886

[26] Zhang, Y., Chen, H., Wang, K., and Wang, M., "Aeroacoustic Prediction of a Multi-Element Airfoil Using Wall-Modeled Large-Eddy Simulation," *AIAA Journal*, Vol. 55, No. 12, 2017, pp. 4219–4233.
doi:10.2514/1.J055853

[27] Broeren, A. P., Bragg, M. B., and Addy, H., "Flowfield Measurements About an Airfoil with Leading-Edge Ice Shapes," *Journal of Aircraft*, Vol. 43, No. 4, 2006, pp. 1226–1234.
doi:10.2514/1.19021

[28] Chen, H., Li, Z., and Zhang, Y., "U or V Shape: Dissipation Effects on Cylinder Flow Implicit Large-Eddy Simulation," *AIAA Journal*, Vol. 55, No. 2, 2017, pp. 459–473.
doi:10.2514/1.J055278

[29] Zhang, Y., Chen, H., Zhang, M., Zhang, M., Li, Z., and Fu, S., "Performance Prediction of Conical Nozzle Using Navier–Stokes Computation," *Journal of Propulsion and Power*, Vol. 31, No. 1, 2015, pp. 192–203.
doi:10.2514/1.B35164

[30] Li, Z., Zhang, Y., and Chen, H., "A Low Dissipation Numerical Scheme for Implicit Large Eddy Simulation," *Computers & Fluids*, Vol. 117, June 2015, pp. 233–246.
doi:10.1016/j.compfluid.2015.05.016

[31] Vreman, A. W., "An Eddy-Viscosity Subgrid-Scale Model for Turbulent Shear Flow: Algebraic Theory and Applications," *Physics of Fluids*, Vol. 16, No. 10, 2004, pp. 3670–3681.
doi:10.1063/1.1785131

[32] Kawai, S., and Larsson, J., "Wall-Modeling in Large Eddy Simulation: Length Scales, Grid Resolution, and Accuracy," *Physics of Fluids*, Vol. 24, No. 1, 2012, Paper 015105.
doi:10.1063/1.3678331

[33] Menter, F. R., "Two-Equation Eddy-Viscosity Turbulence Models for Engineering Applications," *AIAA Journal*, Vol. 32, No. 8, 1994, pp. 1598–1605.
doi:10.2514/3.12149

[34] Lee, S., and Bragg, M. B., "Investigation of Factors Affecting Iced-Airfoil Aerodynamics," *Journal of Aircraft*, Vol. 40, No. 3, 2003, pp. 499–508.
doi:10.2514/2.3123

[35] Marongiu, C., Vitagliano, P. L., Zanazzi, G., and Narducci, R., "Aerodynamic Analysis of an Iced Airfoil at Medium/High Reynolds Number," *AIAA Journal*, Vol. 46, No. 10, 2008, pp. 2469–2478.
doi:10.2514/1.34550

[36] Hunt, J. C. R., Wray, A. A., and Moin, P., "Eddies, Stream, and Convergence Zones in Turbulent Flows," *Proceedings of the Summer Program 1988*, Center for Turbulence Research, Stanford Univ., Rept. CTR-S88, California, Dec. 1988.

[37] Blumenthal, L., Busch, G., Broeren, A., and Bragg, M., "Issues in Ice Accretion Aerodynamic Simulation on a Subscale Model," *44th AIAA Aerospace Sciences Meeting and Exhibit*, AIAA Paper 2006-0262, Jan. 2006.
doi:10.2514/6.2006-262

[38] Gurbacki, H. M., and Bragg, M. B., "Unsteady Aerodynamic Measurements on an Iced Airfoil," *40th AIAA Aerospace Sciences Meeting and Exhibit*, AIAA Paper 2002-0241, Jan. 2002.
doi:10.2514/6.2002-241

[39] Szepessy, S., "On the Spanwise Correlation of Vortex Shedding from a Circular Cylinder at High Subcritical Reynolds Number," *Physics of Fluids*, Vol. 6, No. 7, 1994, pp. 2406–2416.
doi:10.1063/1.868438

[40] Manshadi, M. D., and Esfeh, M. K., "Experimental Investigation of Flowfield over an Iced Aerofoil," *Aeronautical Journal*, Vol. 120, No. 1227, 2016, pp. 735–756.
doi:10.1017/aer.2016.29

[41] Ansell, P., and Bragg, M., "Measurement of Unsteady Flow Reattachment on an Airfoil with a Leading-Edge Horn-Ice Shape," *30th AIAA Applied Aerodynamics Conference*, AIAA Paper 2012-2797, Jan. 2012.
doi:10.2514/6.2012-2797

[42] Gurbacki, H. M., and Bragg, M. B., "Unsteady Flow Field About an Iced Airfoil," *42nd Aerospace Sciences Meeting and Exhibit*, AIAA Paper 2004-562, Jan. 2004.
doi:10.2514/6.2004-562

[43] Mirzaei, M., Ardekani, M. A., and Doosttalab, M., "Numerical and Experimental Study of Flow Field Characteristics of an Iced Airfoil," *Aerospace Science and Technology*, Vol. 13, No. 6, 2009, pp. 267–276.
doi:10.1016/j.ast.2009.05.002

This article has been cited by:

1. Magnus K. Vinnes, R. Jason Hearst. 2021. Aerodynamics of an airfoil with leading-edge icing. *Wind Energy* **24**:8, 795-811. [Crossref]

2. Yufei Zhang, Pu Yang, Runze Li, Haixin Chen. 2021. Unsteady Simulation of Transonic Buffet of a Supercritical Airfoil with Shock Control Bump. *Aerospace* **8**:8, 203. [Crossref]

3. Maochao Xiao, Yufei Zhang. 2021. Improved Prediction of Flow Around Airfoil Accreted with Horn or Ridge Ice. *AIAA Journal* **59**:6, 2318-2327. [Citation] [Full Text] [PDF] [PDF Plus]

4. Young Mo Lee, Jae Hwa Lee, Lawrence Prince Raj, Je Hyun Jo, Rho Shin Myong. 2021. Large-eddy simulations of complex aerodynamic flows over multi-element iced airfoils. *Aerospace Science and Technology* **109**, 106417. [Crossref]

5. Zhao Li, Xiaoyan Tong, Jing Sun, Feng Jiang, Guangjun Yang, Jingping Xiao, Yu Shi. 2020. Methods and Criterion for Adaptive Ice Accretion Simulation: Mesh Boundary Merge and Reconstruction. *International Journal of Applied Mechanics* **12**:09, 2050105. [Crossref]

6. Maochao Xiao, Yufei Zhang. 2020. Assessment of the SST-IDDES with a shear-layer-adapted subgrid length scale for attached and separated flows. *International Journal of Heat and Fluid Flow* **85**, 108653. [Crossref]

7. Haoran Li, Yufei Zhang, Haixin Chen. 2020. Aerodynamic Prediction of Iced Airfoils Based on Modified Three-Equation Turbulence Model. *AIAA Journal* **58**:9, 3863-3876. [Abstract] [Full Text] [PDF] [PDF Plus]

8. Maochao Xiao, Yufei Zhang, Feng Zhou. 2020. Numerical Investigation of the Unsteady Flow Past an Iced Multi-Element Airfoil. *AIAA Journal* **58**:9, 3848-3862. [Abstract] [Full Text] [PDF] [PDF Plus]

9. Shuoyang Bao, Yuejun Shi, Wenbin Song. Numerical Study of Iced Airfoil Aeroacoustics Using IDDES . [Abstract] [PDF] [PDF Plus]

10. Hossein Fatahian, Hesamoddin Salarian, Majid Eshagh Nimvari, Jahanfar Khaleghinia. 2020. Effect of Gurney flap on flow separation and aerodynamic performance of an airfoil under rain and icing conditions. *Acta Mechanica Sinica* **36**:3, 659-677. [Crossref]

11. Haoran Li, Yufei Zhang, Haixin Chen. 2019. Optimization of Supercritical Airfoil Considering the Ice-Accretion Effects. *AIAA Journal* **57**:11, 4650-4669. [Abstract] [Full Text] [PDF] [PDF Plus]